Supporting Information for "First assimilation of atmospheric temperatures from the Emirates Mars InfraRed Spectrometer"

Roland M. B. Young[1,*], Ehouarn Millour[2], François Forget[2], Michael D. Smith[3], Mariam Aljaberi[1], Christopher S. Edwards[4], Nathan Smith[4], Saadat Anwar[5], Philip R. Christensen[5], Michael J. Wolff[6]

[1]Department of Physics & National Space Science and Technology Center, UAE University, Al Ain, United Arab Emirates.
[2]Laboratoire de Météorologie Dynamique (LMD/IPSL), Sorbonne Université, ENS, PSL Research University, École Polytechnique, Institut Polytechnique de Paris, CNRS, Paris, France
[3]NASA Goddard Space Flight Center, Greenbelt, MD, USA
[4]Department of Astronomy and Planetary Science, Northern Arizona University, NAU BOX 6010, Flagstaff, AZ 86011, USA
[5]School of Earth and Space Exploration, Arizona State University, Tempe, AZ, USA
[6]Space Science Institute, Boulder, CO 80301, USA

[*]roland.young@uaeu.ac.ae

Contents of this file

1. Text S1: EXI image processing for Fig. 2 in the main paper

The Level 2A EMM-EXI images have latitude/longitude locations for each pixel. But as each of the four images in the observation (635, 546, 437, and 320 nm) was taken at a slightly different time, the location of each pixel was slightly different for each image. Therefore to create a composite RGB image we must map the individual images to a common grid.

First, all bad pixels (nonzero Data Quality Flag) were removed. Pixels below a dark limit of 30 Data Numbers (DN) were also removed, which removed all pixels not intersecting the planet. Each image was then mapped onto a common longitude/latitude grid with a spatial resolution of 0.1°. This is comparable with the pixel separation at nadir (2–4 km depending on position in the orbit). At each grid point, nearby pixels were identified and the brightness at the grid point was set based on a weighted average of nearby pixels with a weight of r^{-4}, where r is the great-circle distance between the grid point and the pixel. This means the closest pixel is assigned a significantly higher weight than any other pixel, and that the total weight assigned to a ring of width dr at radius r falls with increasing r (this requires the exponent to be more negative than -2). While this method is somewhat *ad hoc*, it ensures smooth transitions in brightness between grid points where there are few nearby pixels, such as near the limb. This is not the case for alternatives such as nearest neighbour mapping. Finally, all missing data and all negative brightnesses were replaced with zero brightness.

To create the colour (RGB) composite, the brightnesses of the three mapped single-filter images (635 nm for red, 546 nm for green, and 437 nm for blue) on the shared 0.1° grid were scaled to 8-bit byte-scaled values between 0 and 255. The maximum DN over all three filters over all eight images was used for 255, and DN = 0 was used for 0. The brightness at each point was linearly interpolated between these limits. The byte-scaled brightnesses in the blue filter were then multiplied by two, and saturated blue points were set to 255. This brought the blue filter frequency distribution and brightness limits closer to those for red and green, and gave water ice clouds a slight blue tint.

The 320 nm images were processed separately. Brightnesses on the 0.1° grid were linearly interpolated to 8-bit values using DN = 400 as the value for 0, and DN = 4000 as the value for 255. The latter is approximately the 99th percentile brightness above DN = 400 over all points in all eight images. This optimized the contrast in the part of the image containing the elongated water ice cloud. The brightness of the first image (taken shortly after sunrise at the inset location in Fig. 2) was also increased by 25% for a smoother transition to later frames in the animation of 320nm images, and for easier comparison of the elongated water ice cloud position with later times.

2. Text S2: List of EXI images used

The list below contains all the images used in Fig. 2 in the main paper and the animated GIFs listed in Section 3. All these images are available via the EMM public archive at https://sdc.emiratesmarsmission.ae.

The images are all Level 2A, and are taken using observation strategy XOS-1 (Jeppesen et al., 2021; Jones et al., 2021). The files are listed in chronological order. The images in each XOS-1 observation set are ordered by red, green, ultraviolet, and blue filters. A fifth image in each XOS-1 observation set was taken using the ultraviolet 260 nm filter, but as this was not used in our analysis it is not listed here.

```
emm_exi_l2a_20210816T140408_0094_xos1_f635_f_v05-01.fits
emm_exi_l2a_20210816T140425_0094_xos1_f546_f_v05-01.fits
emm_exi_l2a_20210816T140433_0094_xos1_f320_f_v05-01.fits
emm_exi_l2a_20210816T140436_0094_xos1_f437_f_v05-01.fits

emm_exi_l2a_20210816T155102_0094_xos1_f635_f_v05-01.fits
emm_exi_l2a_20210816T155119_0094_xos1_f546_f_v05-01.fits
emm_exi_l2a_20210816T155127_0094_xos1_f320_f_v05-01.fits
emm_exi_l2a_20210816T155130_0094_xos1_f437_f_v05-01.fits

emm_exi_l2a_20210816T160602_0094_xos1_f635_f_v05-01.fits
emm_exi_l2a_20210816T160619_0094_xos1_f546_f_v05-01.fits
emm_exi_l2a_20210816T160627_0094_xos1_f320_f_v05-01.fits
emm_exi_l2a_20210816T160630_0094_xos1_f437_f_v05-01.fits

emm_exi_l2a_20210816T162102_0094_xos1_f635_f_v05-01.fits
emm_exi_l2a_20210816T162119_0094_xos1_f546_f_v05-01.fits
emm_exi_l2a_20210816T162127_0094_xos1_f320_f_v05-01.fits
emm_exi_l2a_20210816T162130_0094_xos1_f437_f_v05-01.fits

emm_exi_l2a_20210816T164315_0094_xos1_f635_f_v05-01.fits
emm_exi_l2a_20210816T164332_0094_xos1_f546_f_v05-01.fits
emm_exi_l2a_20210816T164340_0094_xos1_f320_f_v05-01.fits
emm_exi_l2a_20210816T164343_0094_xos1_f437_f_v05-01.fits

emm_exi_l2a_20210816T172353_0094_xos1_f635_f_v05-01.fits
emm_exi_l2a_20210816T172410_0094_xos1_f546_f_v05-01.fits
emm_exi_l2a_20210816T172418_0094_xos1_f320_f_v05-01.fits
emm_exi_l2a_20210816T172421_0094_xos1_f437_f_v05-01.fits

emm_exi_l2a_20210816T173532_0094_xos1_f635_f_v05-01.fits
emm_exi_l2a_20210816T173549_0094_xos1_f546_f_v05-01.fits
emm_exi_l2a_20210816T173557_0094_xos1_f320_f_v05-01.fits
emm_exi_l2a_20210816T173600_0094_xos1_f437_f_v05-01.fits

emm_exi_l2a_20210816T175032_0094_xos1_f635_f_v05-01.fits
emm_exi_l2a_20210816T175049_0094_xos1_f546_f_v05-01.fits
emm_exi_l2a_20210816T175057_0094_xos1_f320_f_v05-01.fits
emm_exi_l2a_20210816T175100_0094_xos1_f437_f_v05-01.fits
```

3. Text S3: Animated GIFs

Three animated GIFs are included with this paper. All three show sequences from the eight EMM-EXI observations listed in Section 2, from 16 August 2021, with the first taken at 14:04 and the last at 17:51. This corresponds to Mars Year 36, $L_s = 86.29 - 86.36°$. There is a gap of 107 minutes between the first and second frames, so that transition is less smooth than the others. Because of pointing limitations the final three frames are slightly misaligned.

`EMM_EXI_RGB_20210816_view_from_EMM.gif`

Composite RGB images (635, 546, and 437 nm) as seen from the point of view of EMM. The only addition is a set of reference gridlines every 30°.

`EMM_EXI_RGB_20210816_inset_orthographic_14h04_to_17h51_with_LETKF_emm009_fields_at_20Pa.gif`

Inset orthographic view of Mars' northern hemisphere centered around the water ice cloud and dusty vortex presented in Fig. 2b in the main paper. The background is the same composite RGB image as above. Grey lines are latitude/longitude gridlines. Black contours show the analysis temperature field at 20 Pa. Black arrows show the analysis horizontal wind field at 20 Pa. The dashed white line is used for the cross-sections in Fig. 2e in the main paper, and is straight in longitude-latitude coordinates.

`EMM_EXI_320nm_20210816_inset_orthographic_14h04m36_to_17h51m00.gif`

320 nm (ultraviolet) imaging showing an inset orthographic view of Mars' northern hemisphere centered around the water ice cloud presented in Fig. 2d in the main paper. Grey lines show longitude/latitude gridlines.

References

Jeppesen, C., Jones, A., Shuping, R., & Wolff, M. (2021). *EXI Data Product Guide* (Document No. 169996). Mohammed bin Rashid Space Centre: Available at https://sdc.emiratesmarsmission.ae.

Jones, A. R., Wolff, M., Alshamsi, M., Osterloo, M., Bay, P., Brennan, N., ... Yaptengco, J. L. (2021). The Emirates Exploration Imager (EXI) Instrument on the Emirates Mars Mission (EMM) Hope Mission. *Space Science Reviews*, *217*, 81. doi: 10.1007/s11214-021-00852-5

4. Figure S1

Number of EMIRS atmospheric temperature profiles as a function of LTST and latitude, between MY36 $L_s = 57.34 - 92.90°$. White regions indicate missing data. Data are binned in 0.5-hour, 5°-latitude bins.

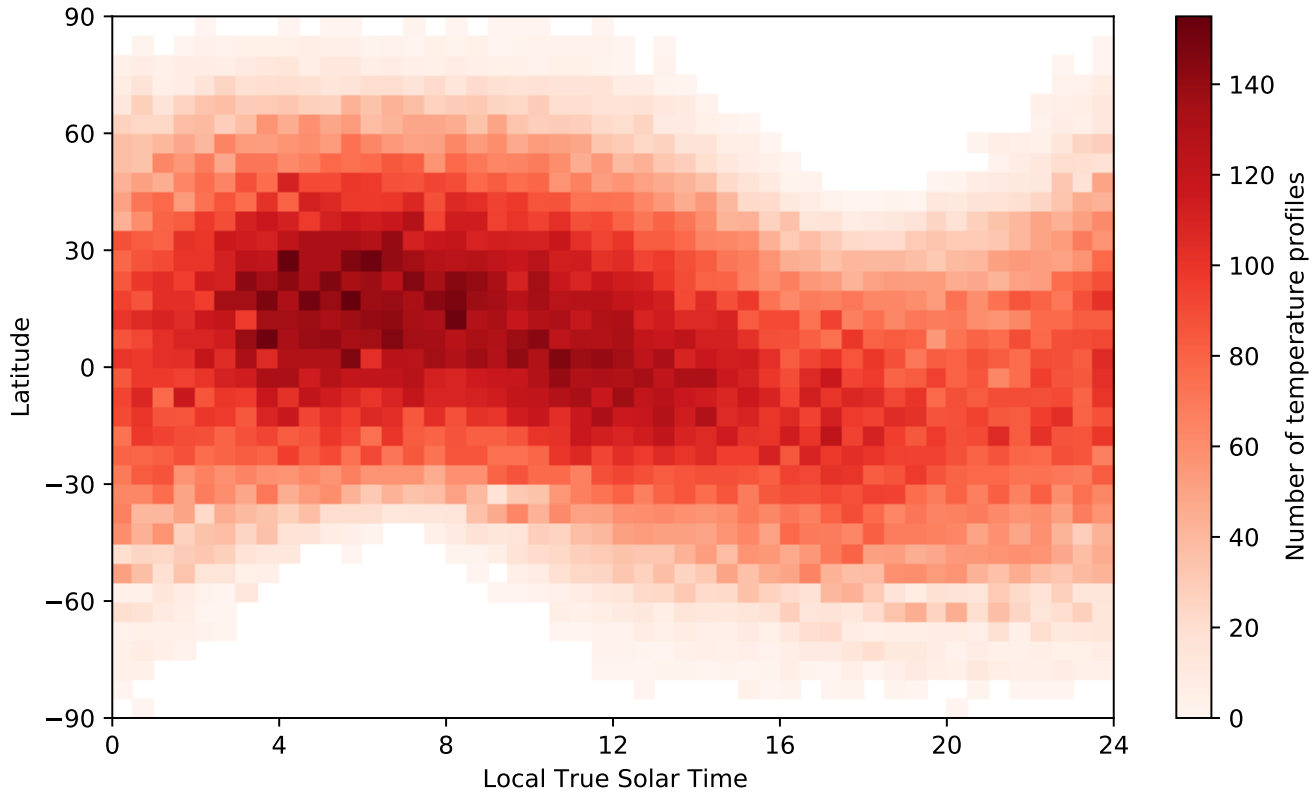

5. Figure S2

Global maps illustrating how EMIRS observes the same location over several hours, from the point of view of the assimilation. The domain is partitioned like the GCM grid: 5.625° in longitude and 3.75° in latitude. Within each grid box we found the distribution of continuous observation periods and the associated observation gaps. A grid box was defined to be observed within a 3-hour period if there were any observations within 900 km of the grid point during this time; this is the criterion used to identify observations near a grid point to assimilate. **(a)** shows the mean period of continuous observation, and **(b)** shows the mean gap between observation periods. All the data from MY36 sol 121 - 1.5 hours up to sol 200 + 1.5 hours were used in the calculation.

(a) Mean continuous observation period.

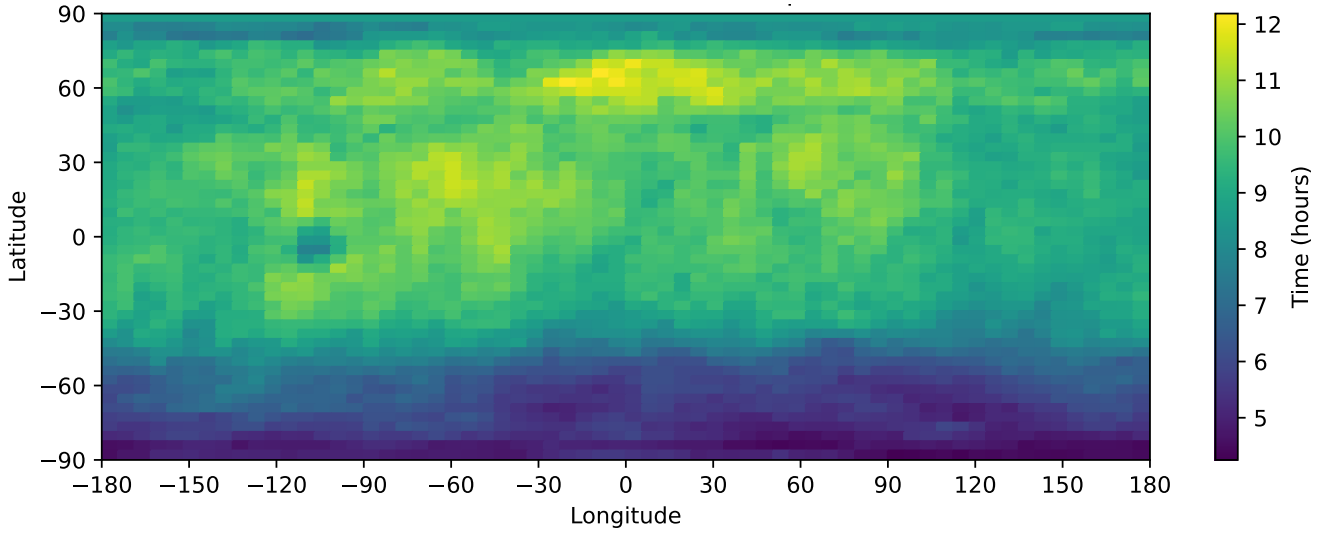

(b) Mean observation gap.

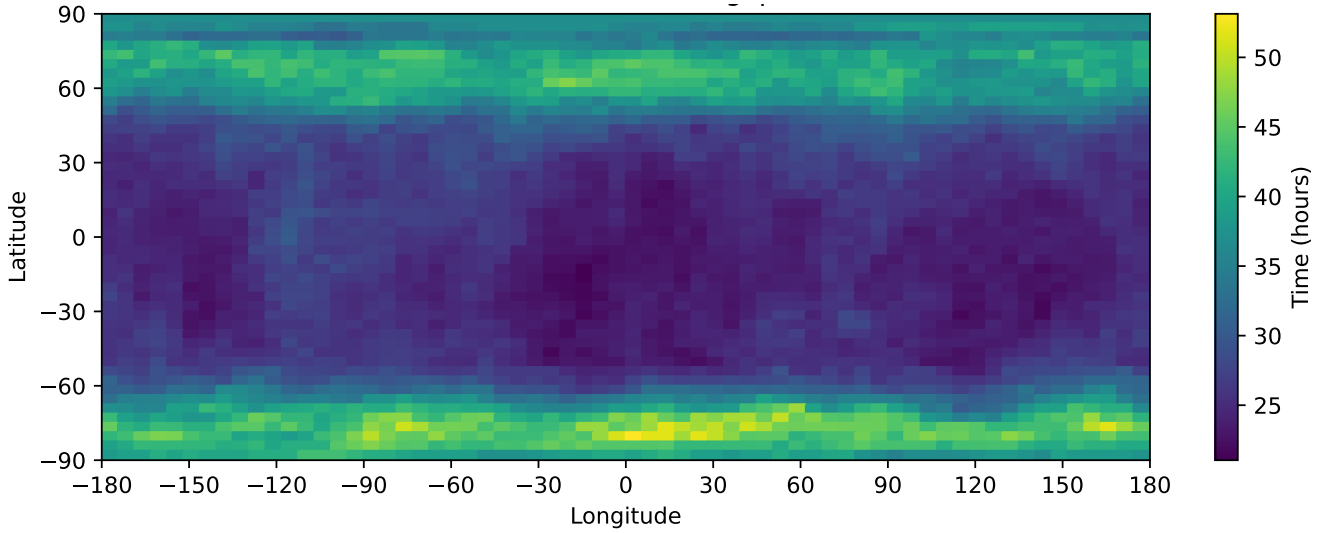

6. Figure S3

Example application of the convolution observation operator to a temperature forecast. In **(a)**, the observed EMIRS temperature retrieval is the series of red dots. The ensemble mean forecast temperature profile is green, and the smoothed ensemble mean forecast is blue. Black dots show vertical locations where the smoothed ensemble mean forecast was sampled for direct comparison with the observed profile. **(b)** shows three example smoothing functions (dimensionless) for model levels at $Z = 0.21$ (red), $Z = 2.12$ (green), and $Z = 4.33$ (blue). The left y-axes show pressure scale heights above the ground, and the right y-axes show atmospheric pressure. This particular EMIRS temperature retrieval is at longitude 112.40°W, latitude 37.30°S, at $L_s = 88.36°$ (equivalent to GCM sol 190.02). It was chosen to illustrate the observation operator and highlight a case where the forecast, smoothed profile, and observations are different. In most cases, the forecast, smoothed profile, and observations are closer together.

(a) Raw and smoothed forecasts, and observations.

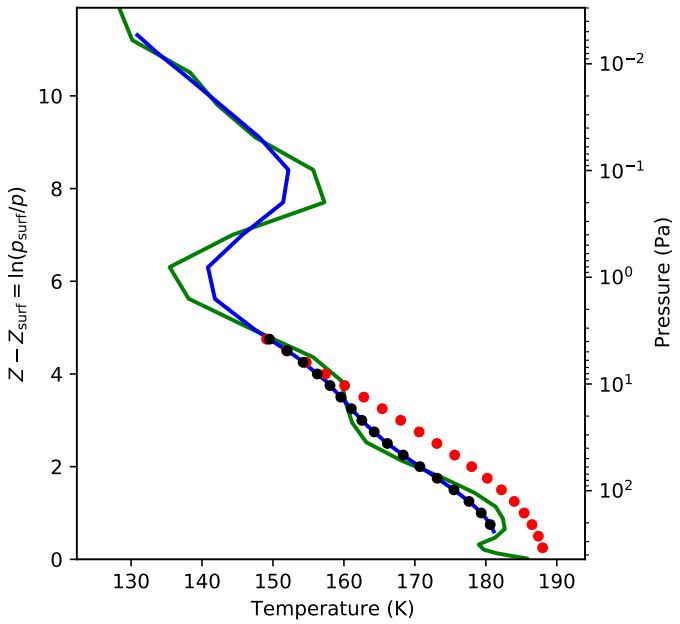

(b) Three vertical smoothing functions.

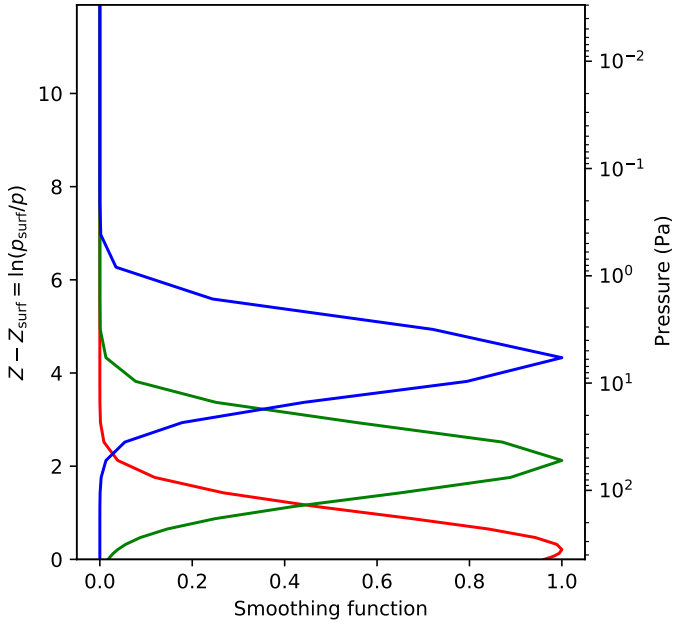

7. Figure S4

As Fig. 1 in the main text, but for the two horizontal velocity components. Data are interpolated vertically to 30 Pa, linearly in $\log p$. **(a)** Zonal velocity forecast, with contours separated by 20 m s^{-1}. **(b)** Meridional velocity forecast, with contours separated by 10 m s^{-1}. **(c)** Zonal velocity analysis, with contours separated by 20 m s^{-1}. **(d)** Meridional velocity analysis, with contours separated by 10 m s^{-1}. **(e)** Zonal velocity increment (analysis minus forecast), with contours separated by 10 m s^{-1}. **(f)** Meridional velocity increment, with contours separated by 5 m s^{-1}. Each figure is a Mollweide projection centered on longitude/latitude zero. The data are from MY36 sol 165.75 ($L_s = 77.50°$). The LTST at longitude zero is 18:00.

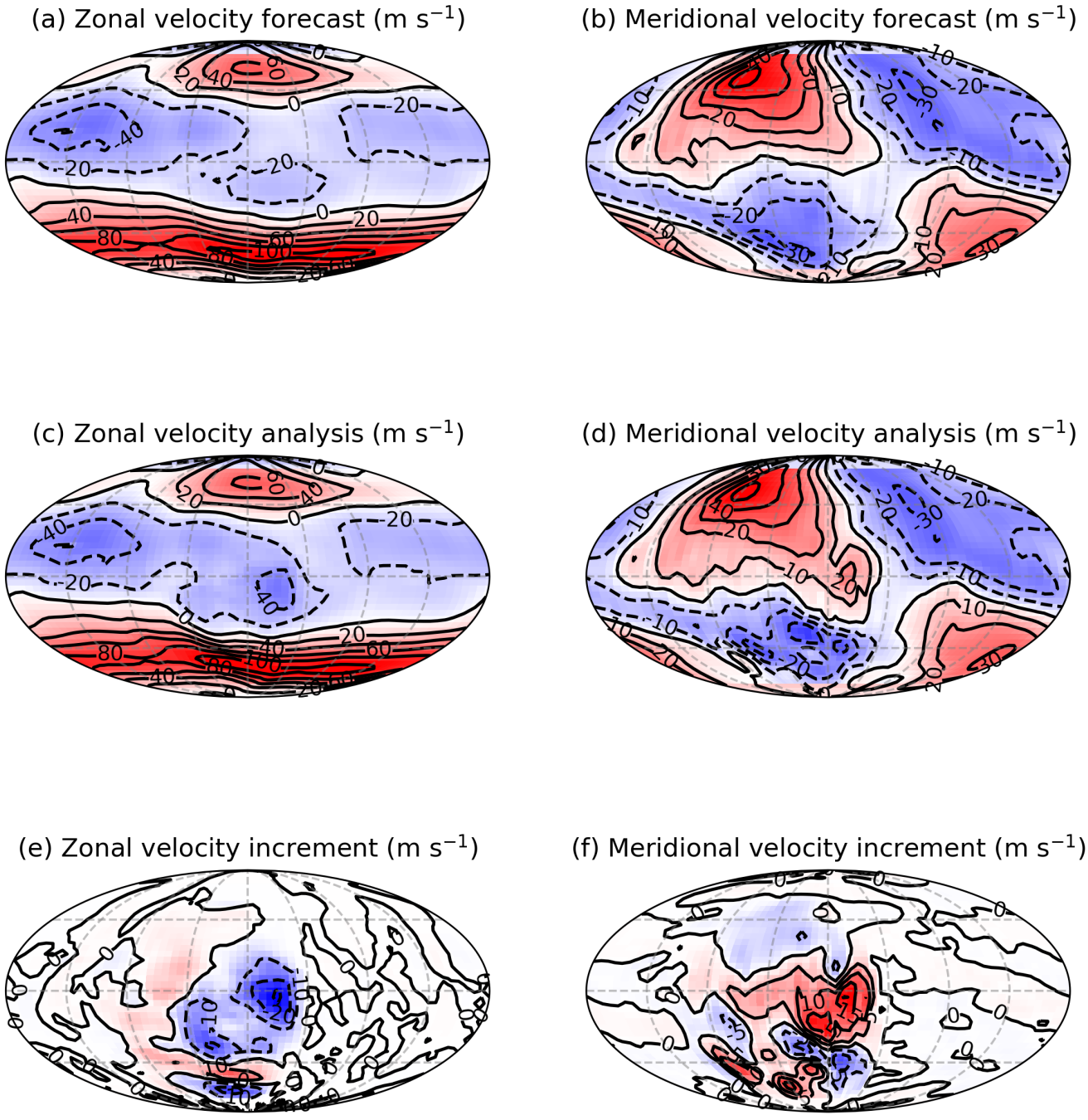

8. Figure S5

Temperature errors compared with EMIRS temperature retrievals between 10–30 km pseudo-altitude. **(a)** shows bias (model minus observations) and **(b)** shows RMS error. In each case black is the forecast mean, blue is the analysis mean, and red is the GCM ensemble mean. Each line shows a 1-sol running mean. Before comparing with observations, the convolution observation operator (Eq. 1) was applied to each forecast/analysis profile. In (b), the green asterisk indicates the temperature uncertainty in this altitude range in the EMIRS dataset.

(a) Bias (model minus observations).

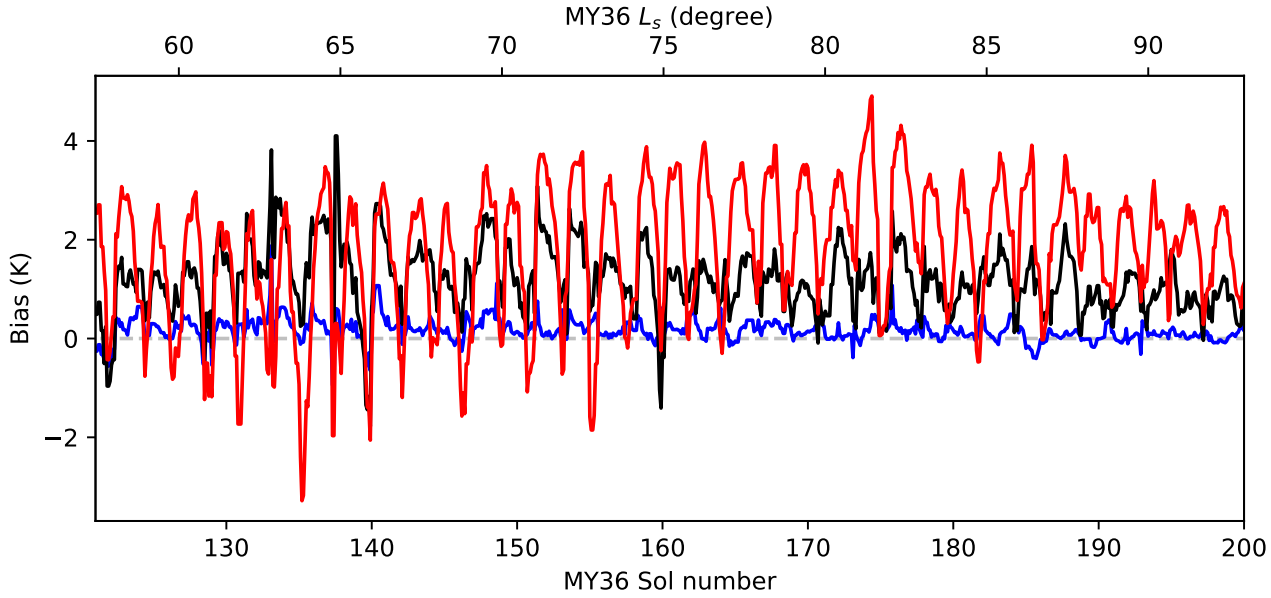

(b) Root-mean-squared error.

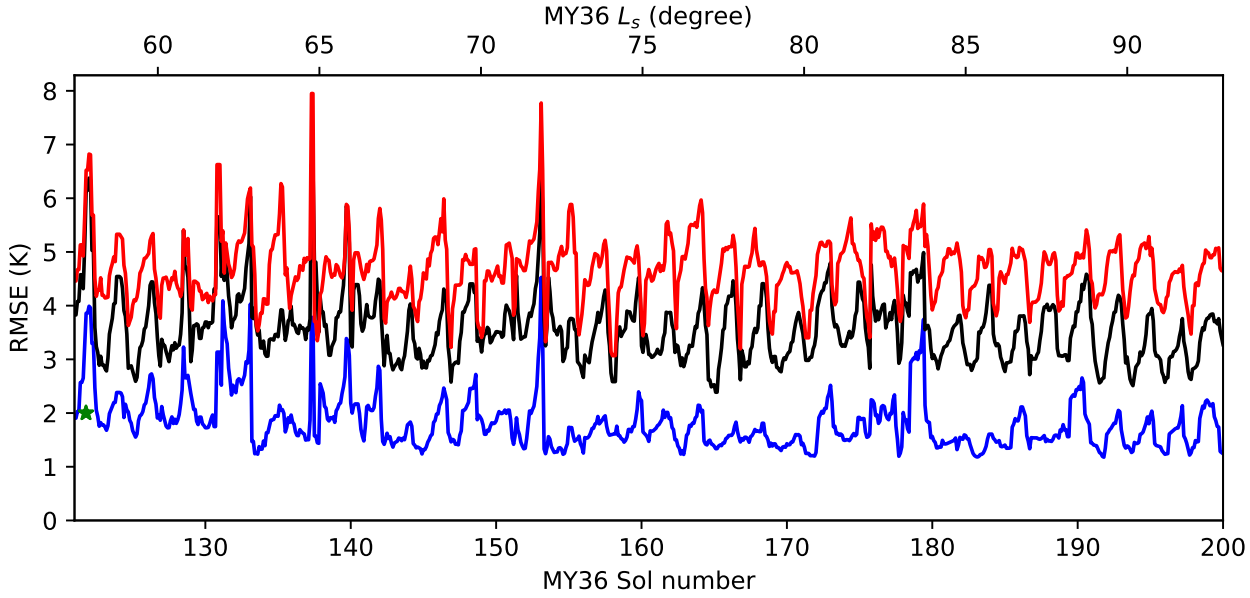

9. Figure S6

As Fig. S4, but showing temperature errors compared with MCS temperature profiles between 100–10 Pa. Because the vertical resolution of MCS observations is comparable with the GCM vertical grid spacing, no vertical smoothing was applied to the forecast/analysis profile before comparing with observations.

(a) Bias (model-observations).

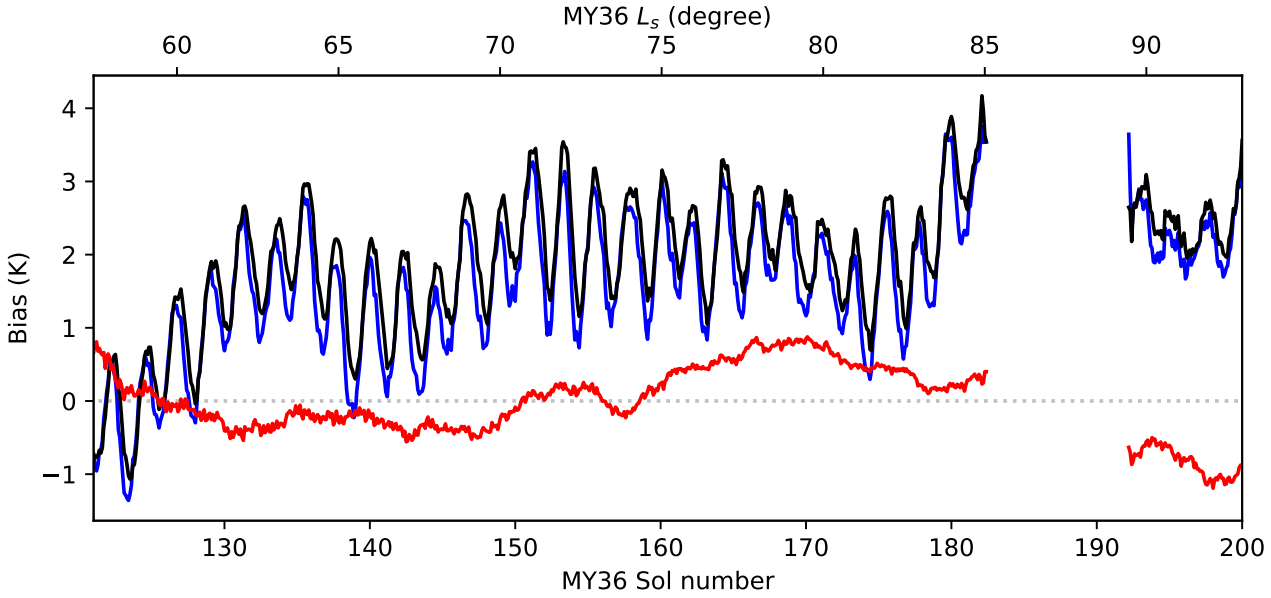

(b) Root-mean-squared error.

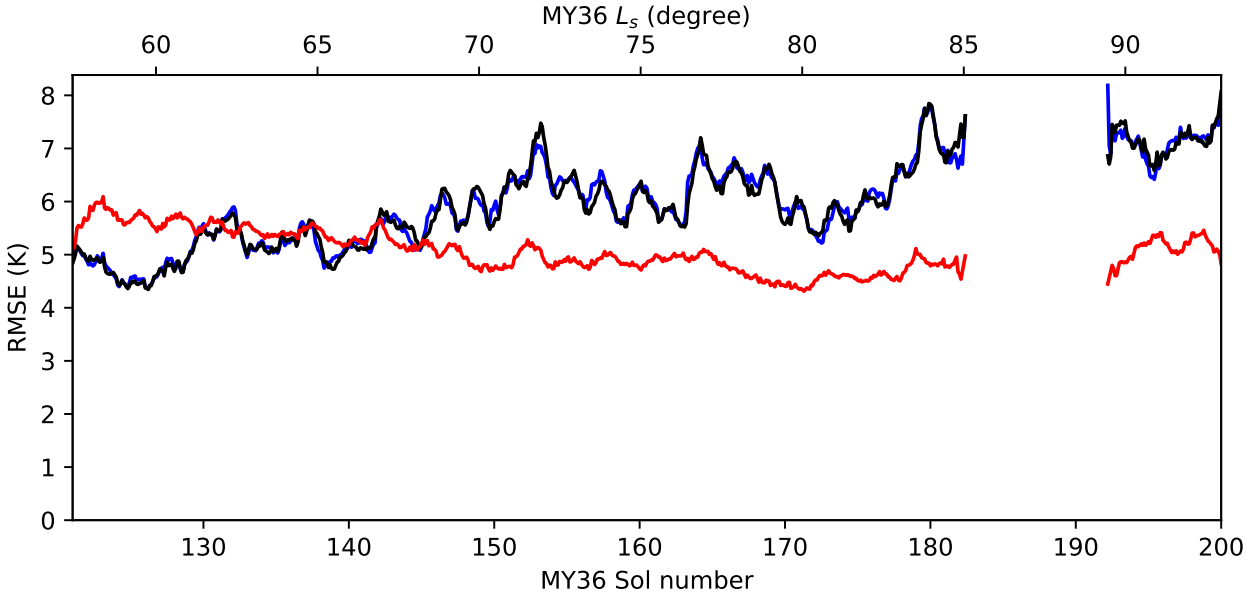

10. Figure S7

As Fig. 3 in the main text, but showing the daily cycle of **(a)** temperature, **(b)** zonal velocity, and **(c)** meridional velocity for the GCM ensemble mean at 30 Pa averaged over $L_s = 60 - 90°$.

(a) Temperature.

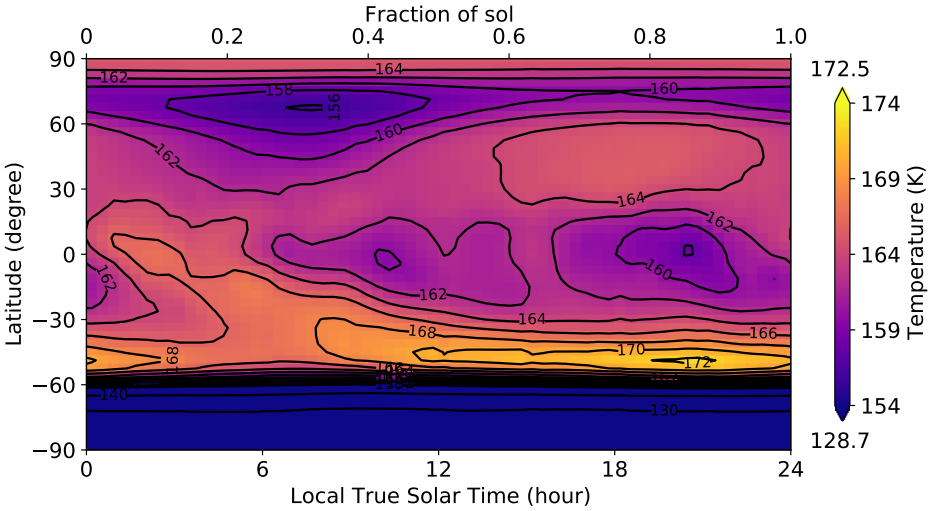

(b) Zonal velocity.

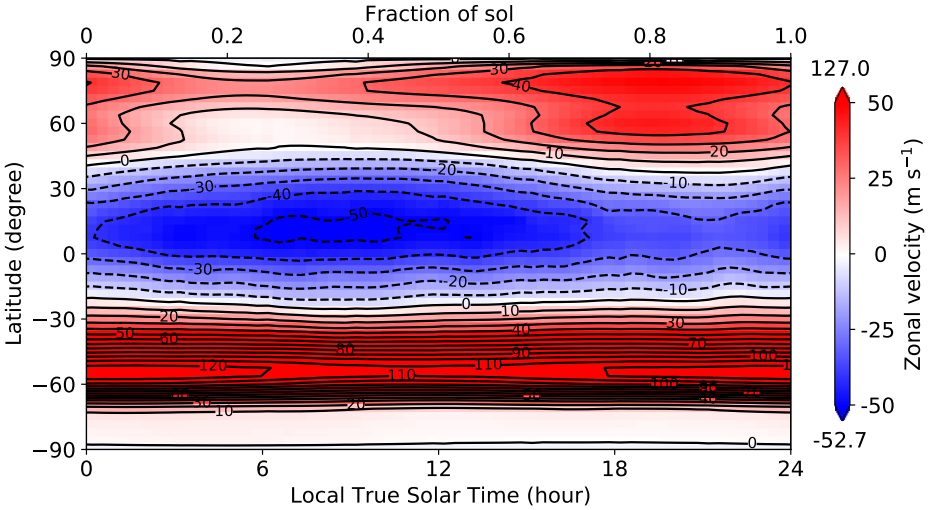

(c) Meridional velocity.

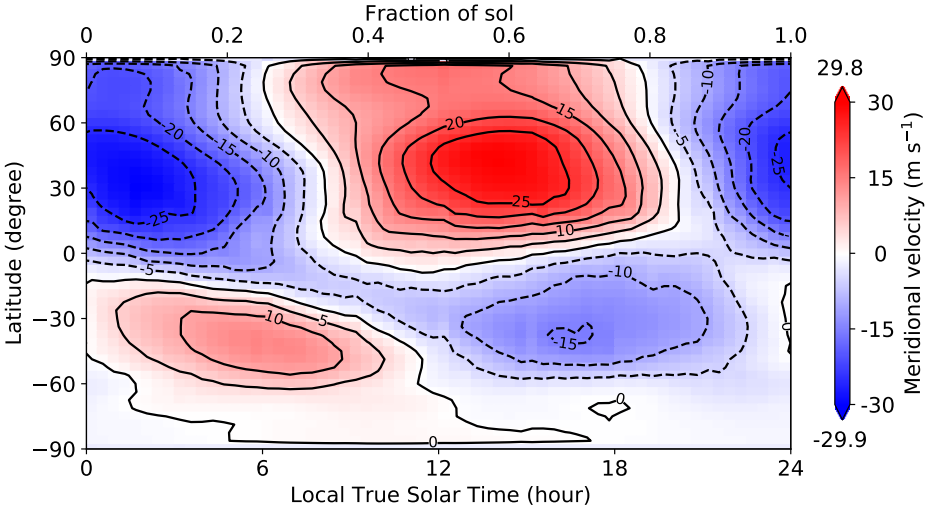

11. Table S1

Summary of verification statistics comparing the assimilation and GCM ensemble with EMIRS and MCS temperature profiles.

In-sample temperature verification vs EMIRS						
	Bias (K)			RMSE (K)		
Pseudo-altitude range (km)	0–10	10–30	30–50	0–10	10–30	30–50
GCM ensemble	2.88	2.15	0.08	5.36	4.74	2.70
Assimilation (forecast)	0.20	1.22	1.73	3.37	3.55	3.95
Assimilation (analysis)	-0.15	0.14	0.66	2.16	1.83	2.50
Independent temperature verification vs MCS						
	Bias (K)			RMSE (K)		
Pressure range (Pa)	1000–100	100–10	10–1	1000–100	100–10	10–1
GCM ensemble	-1.58	0.04	0.65	7.10	5.04	10.28
Assimilation (forecast)	-1.84	1.96	4.27	6.49	6.00	8.63
Assimilation (analysis)	-1.70	1.65	4.12	6.55	6.02	8.55